Optik 73, No. 4 (1986) 146–156 © Wissenschaftliche Verlagsgesellschaft mbH, Stuttgart

Exact filters for general geometry three dimensional reconstruction

George Harauz and Marin van Heel

Fritz-Haber-Institut der Max-Planck-Gesellschaft, Berlin, FRG*)

Received 28 December 1985

Abstract

Filtered back projection is a popular algorithm used for reconstructing the internal structures of objects from their projections, e.g., in medical computerised tomography. The filter functions that have been proposed to date have been derived by analytical considerations of idealised situations of (infinitely) many projections uniformly distributed over a well defined angular range. For all practical geometries, however, "exact" filters may be constructed which perform better than the analytical ones. For nonuniform distributions of projection directions, the exact filter is different for each individual projection. We describe a heuristic approach to generating exact filter functions for problems that are separable into the reconstruction of a series of slices ("tomography") as well as for general "direct" three dimensional reconstruction. We demonstrate the use of these exact filter functions using a new class of phantoms with a predefined power spectrum behaviour, and we evaluate the quality of the reconstructions using a novel Fourier shell correlation function.

Inhalt

Exakte Filter für dreidimensionale Rekonstruktionsverfahren genereller Geometrie. Gefilterte Rückprojektion ist ein populäres Verfahren zur Bestimmung interner Strukturen von Objekten aus dessen Projektionen wie zum Beispiel im Bereich der medizinischen Computertomographie. Die bis jetzt vorgeschlagenen analytischen Filterfunktionen sind aus theoretischen Überlegungen abgeleitet worden für den idealisierten Fall von (unendlich) vielen Projektionen, die über einem genau definierten Winkelbereich uniform verteilt liegen. Für alle praktischen Rekonstruktionsanordnungen können aber „exakte" Filterfunktionen konstruiert werden, die zu besseren Ergebnissen führen als die analytischen Funktionen. Bei nichtuniformen Verteilungen der Projektionsrichtungen wird das exakte Filter für jede Projektion unterschiedlich. Es wird eine heuristische Technik beschrieben zur Erzeugung von exakten Filterfunktionen für sowohl Rekonstruktionsprobleme, die reduzierbar sind zur Errechnung einzelner Schichten des Objektes, als auch für generelle „direkte" 3*D*-Rekonstruktionsanordnungen. Wir demonstrieren den Gebrauch der exakten Filterfunktionen mit einer neuen Klasse von Testobjekten mit vorgegebenem Leistungsspektrum, und wir beurteilen schließlich die Qualität der Rekonstruktionen mit Hilfe einer neuen Fourier-Schalenkorrelationsfunktion.

Introduction

The problem of reconstructing an object from its projections arises in many diverse fields, such as radio astronomy, medical imaging, and electron microscopy. If the projection directions are related to one another by rotation by various angles about a single axis, then the reconstruction problem can be formulated as the estimation of a series of two dimensional (2*D*) density distributions (slices) from one dimensional (1*D*) projections [1, 2, 3, 4]. The density distribution of the three dimensional (3*D*) volume is built up by stacking the 2*D* slices. We refer to this situation as tomography, the best known example of which is X-ray computerised tomography. However, direct 3*D* reconstruction techniques are also of interest, e.g., in medical imaging [5, 6, 7, 8] and in macromolecular structure determination by electron microscopy [9, 10]. In the latter application, macromolecules lie randomly oriented on a support film, and one cannot define a common axis of rotation which would reduce the problem to tomography. The relative orientations of individual projections (macromolecules) can be ascertained using multivariate statistical analysis and classification techniques [11, 12, 13], thus providing the necessary data for performing a three dimensional reconstruction.

Convolution or iterative algorithms can be formulated for general *3D* reconstruction problems in an analogous manner to those used in tomography, although the algorithms are more complex because of the increased complexity of the geometry. We shall focus our attention here on the convolution back projection, or filtered back projection, algorithm first described in [14]. Filtered back projection is attractive for direct 3*D* reconstruction because it requires considerably less computation time than iterative techniques.

In the filtered back projection algorithm, projections are pretreated with a filter before being back projected into the plane or volume being reconstructed. The choice of filter depends on the reconstruction geometry (e.g., limited angular ranges), but may also depend on the amount of noise in the projections, and on the type of object being reconstructed. Most published correcting or filter functions have been derived analytically from theo-

*) Faradayweg 4–6, D-1000 Berlin 33, West Germany.

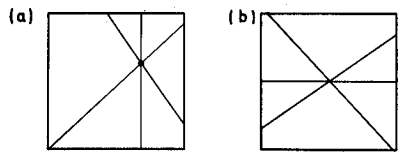

Fig. 1.

(a) Back projection in real space can be thought of as smearing back the projection densities through the higher dimension image being reconstructed. Here an image of a point is reconstructed from 3 projections by back projection and summation.

(b) Back projection in Fourier space can be thought of as the superposition and summation of central sections.

retical considerations [e.g., 14, 15, 16]. An implicit assumption in such derivations is that an infinite number of projections are available, in directions uniformly distributed over some very well defined angular range. This assumption is never strictly true, and in practice one may have only of the order of 5 to 50 projections, in directions sparsely, and possibly randomly, distributed over the unit semicircle or unit hemisphere [17, 18, 19]. In this paper, we describe a heuristic approach to computing filter functions that are exact for each projection in any given reconstruction geometry, either in tomography or in direct $3D$ reconstruction.

The filtered back projection algorithm

It is worthwhile first to review briefly the filtered back projection algorithm [1, 2, 3, 4, 14]. The basis of all real space reconstruction algorithms is back projection. This operation can be thought of as uniformly smearing back, or projecting back, the density from each pixel of the projection image, along the projection direction, into the higher dimension image or volume to be reconstructed. The summation of these back projections represents an approximation to the original image. However, each point in the image will be blurred to a star shape (fig. 1 a), and a correction function must be applied to the projections before back projecting. The projection can be convolved with a correcting function, or equivalently, its Fourier transform can be multiplied by a filter function; hence the names convolution back projection, or filtered back projection.

The form of the filter function can be deduced by considering the problem in Fourier space. By the Projection Theorem, the Fourier transform of each projection represents a central section at the appropriate orientation through the Fourier transform of the object to be reconstructed [20]. The sum of these known sections of the Fourier transform is called a layergram [21] (fig. 1 b). With a small number of projections, there are gaps in the Fourier transform at higher spatial frequencies. These gaps are gradually filled in as more and more projections are used [22, 23].

By considering the inverse of the Projection Theorem, viz., the Back Projection Theorem [5, 24], the transform of the result of a single back projection is zero everywhere except on the plane in frequency space that is perpendicular to the direction of back projection. Thus, the layergram is the Fourier transform of the reconstruction formed by back projection and summation. It can be seen that such a reconstruction is blurred because the low frequency image components are overemphasised compared to the high frequency components. In other words, the density of measurements in Fourier space is greater at lower frequencies. In particular, the zero frequency component (the average density) is enhanced by a factor equal to the number of projections.

Considering the tomographic reconstruction of a point, in the limit of an infinite number of projections with directions uniformly distributed over the unit semicircle, the layergram (i.e., point spread function) comes to resemble a function proportional to $1/f$, where f is the radial frequency. This is because the limiting case of superposition of a number of equally spaced straight lines through the origin is equivalent to rotation of the line about the origin (fig. 1 b) [2, 4]. The weight of each point of the straight line is distributed during rotation along the length of a circumference $2\pi f$. Thus, for tomography, the basic correcting filter function for each $1D$ projection has the form $|f|$. By similar reasoning, the basic filter function for $2D$ projections in direct $3D$ reconstruction has the general form $|f|^2$. Analytical derivations of the corresponding real space correcting functions for both tomography and direct $3D$ reconstruction can be found in Tanaka [16]. The analytical filters used in practice have undergone frequency space modifications by multiplication by windows such as rectangular, Hamming, sinc, or generalised [c.f., 25–30], in order to ameliorate the effects of noise and ringing artefacts.

In most applications of the filtered back projection algorithm in tomography, the same filter function is used for each $1D$ projection. Correct filter functions for situations where the tomographic projection directions are limited to well defined angular ranges have been presented [15]. In direct $3D$ reconstruction for fixed geometries in medical imaging [6, 7, 8], where the projection direction is described by two polar angles, the filter functions derived are dependent on one (but not both) of these polar angles. A similar result holds for the case of "conical tilting" described in an electron microscopy application [31].

In both tomographic and direct $3D$ reconstruction of macromolecular structure from electron micrographs [e.g., 17, 18, 19], one encounters the situation of having few available projections and possibly at directions not uniformly distributed. This problem must especially be considered in direct $3D$ reconstruction. In such a general geometry, one does not necessarily have any symmetry that can be exploited, and the filter function varies from projection to projection, depending on the direction of all the projections that have been measured [5]. We have devised an approach of determining the density of measurements as a function of spatial frequency, based on one projection's orientational relationship to all other projections. The correcting filter functions are based on this

density, and are exact for each projection. In the following sections, we describe in detail how to compute these general filters.

Exact filter functions for tomography

We shall first consider the situation of tomography, as it forms the basis for subsequent consideration of the direct $3D$ case. Say we have N $1D$ projections in directions described by the tilt angles $\theta_1, \theta_2, \ldots, \theta_N$. Each projection consists of n pixels of size s, and consequently the maximum spatial (Nyquist) frequency in these data is $1/2s$. Say the $2D$ object to be reconstructed has a diameter of roughly D, and is contained within an image of $n \times n$ pixels, each also of size s, i.e., $D \leq ns$. During the back projection process, the density from each pixel of the i'th projection is projected back uniformly over a distance D, along the direction θ_i. This back projected function represents a slice of width d^*, at an angle θ_i, of the $2D$ Fourier transform of the image to be reconstructed [22].

The width d^* of the central section is only a characteristic distance describing the size of the convolution volume in Fourier space due to the space-boundedness of the object [22], described by some mask function. The further away we are from the central section, the less its influence is felt (fig. 2a). The exact influence profile of the central section is directly related to the Fourier transform of the mask function. A simple and physically rational profile is the triangle function (fig. 2b), implying that we use a squared sinc mask function [32]. The triangle function has the advantages that it can be calculated quickly and that, in the limiting case of $d^* = 1$, its effect becomes identical to that of the well known linear interpolation scheme. Other real space mask functions lead to different central section profile functions in Fourier space, e.g., a rectangular mask leads to a sinc function [32].

Let us consider projection "i". If only this projection was back projected, the resulting central section (in Fourier space) would contain correctly weighted Fourier coefficients. We are, however, also going to back project all other measured projections "j" ($j \neq i$). The other central sections j will all, to a certain extent, overlap (interact) with central section i, thus leading to an overweighting of the Fourier coefficients in the overlap areas. The overweighting can be predicted, however, and compensated for by filtering projection i (i.e., multiplying in Fourier space) with the inverse of the calculated interaction function.

In calculating the interaction function, we shall only consider positive frequencies f, as values for negative frequencies follow by symmetry. We first derive the weighting function due to the interaction of section j with section i. Let θ_{ij} be the angle between projections i and j, such that $0 \leq \theta_{ij} \leq \pi/2$. From fig. 2a and elementary trigonometry, we see that the overweighting in central section i due to the influence of central section j is described by:

$$I_{ij}(f) = T(Df \sin(\theta_{ij})) \tag{1}$$

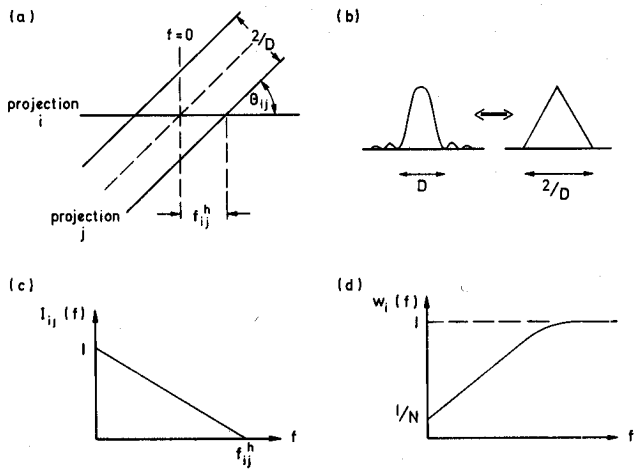

Fig. 2.
(a) The interaction in Fourier space of 2 central sections at a relative angle of θ_{ij}. In our formulation, central section j does not influence central section i beyond the characteristic frequency f^h_{ij}.
(b) The triangle function and the sinc squared function form a Fourier transform pair. The values $2/D$ and D characterise the spatial extent of each function.
(c) Graph of the function describing the interaction of the central sections in (a).
(d) Sketch of an exact filter function for many projection angles.

where T represents the triangle function. In this formulation, it follows that central section j no longer influences central section i beyond the frequency:

$$f^h_{ij} = d^*/\sin\theta_{ij} \tag{2}$$

Below this frequency, the extent of overlap can be described by a linear relationship. Thus, for projection i, we can define an "interaction function" describing its overlap with projection j (fig. 2c):

$$I_{ij}(f) = \begin{cases} 1 - (f/f^h_{ij}) & 0 \leq f \leq f^h_{ij} \\ 0 & f > f^h_{ij} \end{cases} \tag{3}$$

By extension, then, the function describing the overlap of central section i with all other central sections is:

$$I_i(f) = 1 + \sum_{\substack{j=1 \\ j \neq i}}^{N} I_{ij}(f) \tag{4}$$

where the unity value represents the i'th projection's overlap with itself. This function quantifies the overrepresentation of frequency f in the final layergram, i.e., the density of projection measurements at this spatial frequency. Thus, the appropriate corrective filter to be applied to projection i is simply the inverse:

$$W_i(f) = 1/I_i(f) \tag{5}$$

The filtering operation is performed by Fourier transforming each projection, multiplying by the corresponding window function in (5), and inverse transforming.

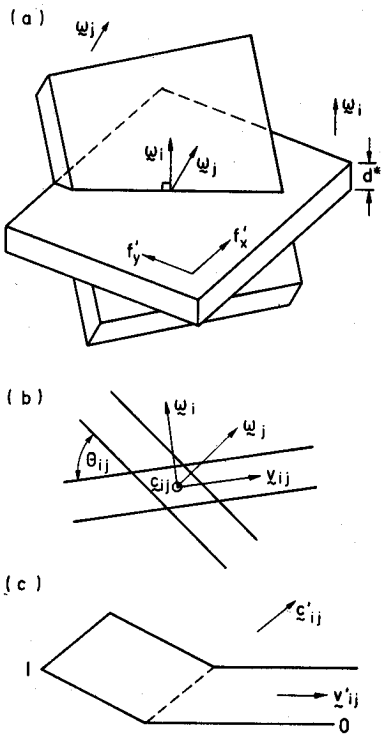

Fig. 3.
(a) The intersection in Fourier space of 2 central sections in a direct $3D$ reconstruction problem.
(b) The direction vectors $\underset{\sim}{\omega}_i$ and $\underset{\sim}{\omega}_j$ define a plane within which the direct $3D$ problem can be viewed as a local tomography problem.
(c) In particular, the cross products of these direction vectors can be used to define vectors $\underset{\sim}{\varsigma}'_i$ and $\underset{\sim}{\nu}'_i$ in whose directions the interaction (overlap) function is constant and variable, respectively.

Back projection and summation are then performed as usual.

The window function in equation (5) has its lowest value $(1/N)$ at zero frequency, and rises monotonically to a value no greater than unity at high frequencies (fig. 2d). In contrast, the analytical (Ramachandran-Lakshminarayanan ramp [14]) filter function:

$$W_{1D}(f) = f/f_N \tag{6}$$

rises linearly from 0 at zero frequency to a value of 1 at the Nyquist frequency. The different response of the two filter functions at zero frequency is noteworthy: The exact filters correctly attenuate this component by the number of projections, whereas the analytical filter simply zeroes this component and thus forces the average density in the projection always to be zero.

Exact filter functions for direct $3D$ reconstruction

Exact filter functions for $2D$ projections in direct $3D$ reconstruction are generated in a similar manner as in tomography, although the geometry is somewhat more complex. We shall assume that we have N $2D$ projections, and that they are square and digitised with pixels of size $s \times s$. These $2D$ images are projections of density of a $3D$ object viewed at an orientation which can be described by the Euler angles (α, β, γ) [9]. The Euler angle α is radial and β is azimuthal. The third Euler angle γ describes a rotation in the projection plane and is required in $3D$ reconstruction of macromolecules from electron micrographs. The transformation from the reference axes of the $3D$ reconstruction to the local coordinate frame of projection i is achieved by the rotation matrix:

$$\underset{\sim}{R}_i = \begin{bmatrix} \cos\gamma_i & \sin\gamma_i & 0 \\ -\sin\gamma_i & \cos\gamma_i & 0 \\ 0 & 0 & 1 \end{bmatrix} \times \begin{bmatrix} 1 & 0 & 0 \\ 0 & \cos\beta_i & \sin\beta_i \\ 0 & -\sin\beta_i & \cos\beta_i \end{bmatrix} \times \begin{bmatrix} \cos\alpha_i & \sin\alpha_i & 0 \\ -\sin\alpha_i & \cos\alpha_i & 0 \\ 0 & 0 & 1 \end{bmatrix} \tag{7}$$

which describes the three successive rotations by these Euler angles. The direction vector of the i'th projection is:

$$\underset{\sim}{\omega}_i = \begin{bmatrix} \sin\alpha_i & \sin\beta_i \\ -\cos\alpha_i & \sin\beta_i \\ \cos\beta_i \end{bmatrix} \tag{8}$$

where the 3 components are the direction cosines of the projection.

As before, we shall consider two projections, i and j, whose Fourier transforms represent central sections of the total $3D$ Fourier transform. We picture the interaction between two slabs of finite width as shown in fig. 3a. The function describing the extent of overlap of projection j with projection i will clearly be constant along one direction, and varying along the perpendicular direction in the plane with a form equivalent to that previously derived for the tomography case (fig. 3b, 3c).

To describe the interaction function, we need the sine of the angle θ_{ij} between the two projections. This value is obtained from the vector product of the i'th and j'th direction vectors:

$$\sin\theta_{ij} = |\underset{\sim}{\omega}_i \times \underset{\sim}{\omega}_j| \tag{9}$$

This value defines the characteristic frequency of the overlap between projections i and j, as in equation (2).

The normalised cross product (or vector product) between the i'th and j'th direction vectors gives a vector parallel to the direction in which the interaction function is constant:

$$\underset{\sim}{\varsigma}_{ij} = \underset{\sim}{\omega}_i \times \underset{\sim}{\omega}_j / (\sin\theta_{ij}) \tag{10}$$

The vector product of the i'th direction vector with the vector in equation (10) gives a vector parallel to the direction in which the interaction function varies:

$$\underset{\sim}{\nu}_{ij} = \underset{\sim}{\omega}_i \times \underset{\sim}{\varsigma}_{ij} \tag{11}$$

Since the vectors in equations (10) and (11) are described with respect to the reference axes, we must con-

vert them to the coordinate system of the i'th projection by multiplying by the rotation matrix:

$$\underset{\sim}{\varrho}'_{ij} = \underset{\sim}{R}_i \underset{\sim}{\varrho}_{ij}$$
$$\underset{\sim}{v}'_{ij} = \underset{\sim}{R}_i \underset{\sim}{v}_{ij} \tag{12}$$

Each point in the $2D$ Fourier transform of projection i is described by the coordinates (f'_X, f'_Y), represented with respect to a standard Cartesian coordinate system. This point can be equivalently represented in a rotated coordinate system described by the "constant" and "variable" vectors:

$$\begin{bmatrix} f'_X \\ f'_Y \end{bmatrix} = f'_V \underset{\sim}{v}'_{ij} + f'_C \underset{\sim}{\varrho}'_{ij} \tag{13}$$

Inverting equation (13) gives the coordinates (f'_V, f'_C) of this particular point with respect to the new coordinate system. The value of f'_C is unused, but the value of f'_V substituted into equation (3) gives the value of the interaction function between the i'th and j'th projections for this point. This calculation is done for each point in the plane, giving a $2D$ interaction function for each $2D$ projection. This interaction function is then inverted to give the exact $2D$ filter for this particular projection. Note that if one has a set of projections with directions lying along a grand circle of the unit sphere, then the filter functions obtained by the analysis described here would be identical to those that would be obtained using the approach for pure tomography described in the previous section.

As for the $1D$ exact windows, the $2D$ exact windows have a minimum value of $1/N$ at zero frequency, and rise monotonically with increasing radial frequency to a maximum value no greater than 1. The $2D$ exact filter function is in general not circularly symmetric. The analytical $2D$ filter function is circularly symmetric, though:

$$W_{2D}(f) = \begin{cases} (f/f_N)^2, & f \leq f_N \\ 1 \quad , & f > f_N \end{cases} \tag{14}$$

being naught at zero radial frequency f, and rising to 1 at the Nyquist frequency. Note that although the maximum frequency along the (orthogonal) axes of digitisation is the Nyquist frequency, we can have radial frequencies of magnitude greater than this in the directions of the corners. Since these frequencies nonetheless represent real information in the image, we set the window to be unity in this region.

Evaluation of exact filters – Methods

Much of the reconstruction literature contains examples of reconstructions using test images that comprise simple objects with sharp edges such as spheres, blocks, head phantoms, etc. Fundamentally, such images contain much very low frequency information, and also some very high frequency information due to the edges. Moreover, the large variety of such test objects makes it difficult to compare the results of different authors, and we wish to propose here an entirely different sort of phantom that can provide a basis for standardisation in the future. The advantages of such a test object are reproducibility and flexibility. The manner of its computation can be described precisely, and it is possible to define the power spectrum to match any situation of interest [33].

Our first $3D$ test image of $48 \times 48 \times 48$ voxels was generated as follows. Each voxel was assigned a random number with a Gaussian distribution (mean zero, standard deviation 10) using a machine independent random number generator (source code is obtainable from the authors upon request). The entire real space volume was then multiplied by a spherically symmetric Gaussian function:

$$G(x, y, z) = \exp(-(x^2 + y^2 + z^2)/u^2) \tag{15}$$

with $u = 14.4$. This operation serves to mask the $3D$ image, i.e., set the voxels at the edges to very small values, as these voxels are not of interest anyways. We shall henceforth refer to this test image as "phantom A". Since no frequency space manipulation of this first phantom was performed, all spatial frequencies are uniformly represented ("white" spectrum).

A second test object (phantom B) was generated as follows. As before, a $3D$ image generated with each voxel being assigned a random number with a Gaussian distribution (the same sequence of numbers that was used for phantom A). The $3D$ Fourier transform was calculated, and multiplied by a spherically symmetric Gaussian function (equation (15)) with $u = 12$. The inverse $3D$ Fourier fransform was computed, and finally this real image was masked by multiplication by another Gaussian function with $u = 12$. This phantom differs from phantom A in that it contains considerably less high spatial frequency information, and is somewhat smaller in size.

From each of the $3D$ phantoms, a total of 59 $2D$ forward projections were generated at Euler angles taken from a real experimental situation: the reconstruction of the nucleosome complex from electron micrographs [10, 18]. These projection directions were sparsely and not uniformly distributed on the unit hemisphere. In another experiment, a total of 200 projections of each $3D$ phantom were generated in directions quasi-uniformly distributed on the unit hemisphere. A truly uniform distribution of projection directions can only be achieved for a low number of projections (3, 4, 6, and 10) by choosing the direction vectors to coincide with the vertices or faces of a regular polyhedron [5, 22]. For the 200 projections, we used a computational method similar to those used in [5, 9] to divide the unit hemisphere into approximately uniform patches. All forward projections were calculated using a bilinear interpolation scheme as described in [34]. A number of these $2D$ projections are shown in fig. 4, and the distributions of projection directions are shown in fig. 5.

Three dimensional reconstructions were computed using both a $2D$ analytical (equation (14)) filter and the $2D$ exact filter functions generated computationally for each projection. Some examples of the exact filters for both reconstruction situations (59 or 200 projections) are

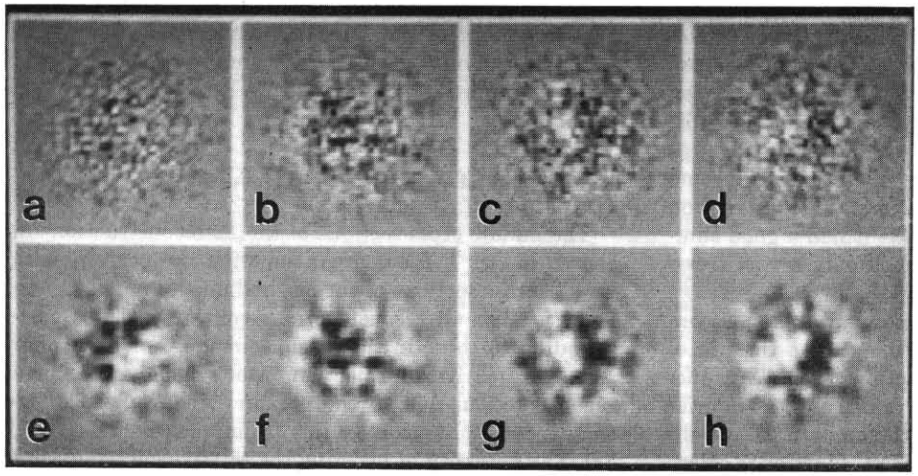

Fig. 4.
(a) Cross-section of phantom A. Projection images of phantom A at Euler angles (in degrees) (b) (180, 142, 53), (c) (349, 65, 165), and (d) (165, 93, 233).
(e) Cross-section of phantom B. Projection images of phantom B at Euler angles (f) (180, 142, 53), (g) (349, 65, 165), and (h) (165, 93, 233).
For display in this figure only, the various images have been scaled to the same background density and variance.

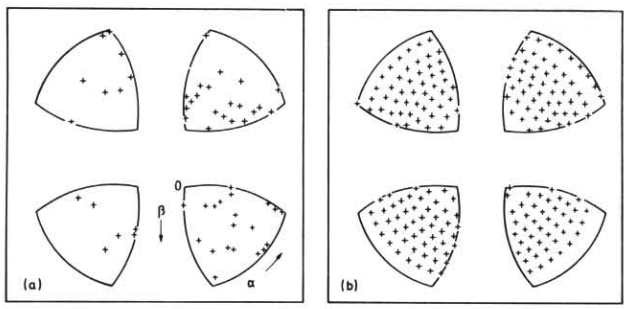

Fig. 5. Distribution of projection directions, i.e., Euler angles (α, β), for the two test geometries described in this paper, with (a) 59 and (b) 200 projections. In 4 instances in (a), two directions nearly coincide and appear as one. The 4 quadrants of the unit hemisphere have been separated and lifted to give a less distorted $2D$ rendition. The top of the hemisphere, marked by an "0", is the point (0,0). The value of β increases along lines of longitude. Along lines of latitude, β is constant, but α changes. The third Euler angle, γ, is not represented here.

shown in fig. 6. For comparison, $3D$ reconstructions were also performed using simple back projection with no prior filtering of the projections. Thus, a total of $2 \times 2 \times 3 = 12$ direct $3D$ reconstructions were performed.

In order to compare the reconstructed images with the original image, we first used some simple picture distance measures found in the literature. One of these was the cross-correlation coefficient [9]:

$$CCC = \frac{\sum_{xyz} (D_1(x,y,z) - \bar{D}_1)\,(D_2(x,y,z) - \bar{D}_2)}{\left(\sum_{xyz} (D_1(x,y,z) - \bar{D}_1)^2 \sum_{xyz} (D_2(x,y,z) - \bar{D}_2)^2\right)^{1/2}} \tag{16}$$

where the sums were over all voxels within a radius of 22 voxels from the origin, and the subscripts 1 and 2 refer to the original and reconstructed image respectively. A value

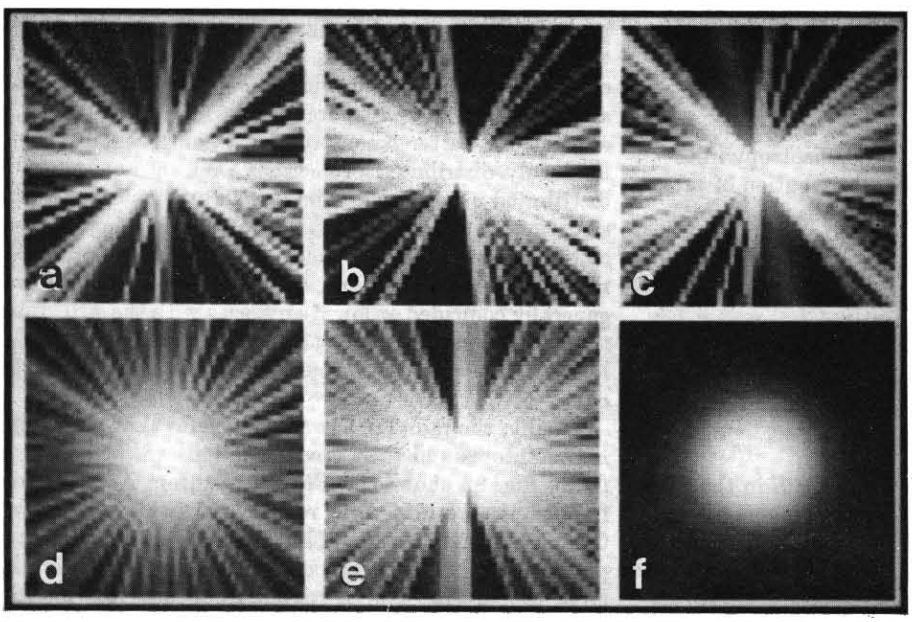

Fig. 6.
(a–c) Examples of exact filters for direct $3D$ reconstruction from 59 projections. The filters correspond to the projections with Euler angles (in degrees) (a) (2, 307, 1), (b) (261, 100, 350), and (c) (80, 275, — 35).
(d, e) Examples of exact filters for direct $3D$ reconstruction from 208 projections. The filters correspond to the projections with Euler angles (d) (346, 38, 0) and (e) (262, 79, 0). Even with 200 projections, there are regions in Fourier space where the projections do not overlap with each other, and the value of the exact filter functions in such regions is unity (dark regions), although the net effect is negligible.
(f) Analytical filter (equation (14)) for direct $3D$ reconstruction.
For display in this figure only, the various images have been scaled nonlinearly to enhance the lower gray values.

of 1 for this coefficient signifies perfect correlation between the two images; a value of 0 represents no correlation; a value of -1 represents anticorrelation. We also used other measures such as the normalised root mean square distance [4], the normalised mean absolute distance [4], and the similarity ratio [35]. We found, however, that these other measures gave no more information than the cross-correlation coefficient, i.e., a reconstruction with a good cross-correlation coefficient had a good similarity ratio, and so on. Thus, we shall only report cross-correlation coefficients here.

A more informative means of comparing the reconstructed images with the original image was the use of Fourier shell correlation (*FSC*) functions. The *FSC* functions are a generalisation to three dimensions of Fourier ring correlation functions used in the analysis of two dimensional images [36, 37, 38]. The *FSC* function is calculated by conjugate multiplying the 3*D* Fourier components of the two images and summing these over spherical shells in Fourier space. The sums per shell are normalised by the square root of the power in the corresponding shell of each of the transforms:

$$FSC(S) = \frac{\sum_{R=S} F_1(R)\, F_2^*(R)}{\left(\sum_{R=S} |F_1(R)|^2 \sum_{R=S} |F_2(R)|^2 \right)^{1/2}} \qquad (17)$$

where S is the radius of the shell, and the subscripts 1 and 2 denote the original and the reconstructed image respectively. Since the two images are real, their Fourier transforms have even real and odd imaginary components. The imaginary component of the *sum* in the numerator of equation (17) (but not of each individual term being summed) is thus zero, and the *FSC* function is a real function. The *FSC* function provides us with a measure of the similarity (viz., correlation) between two images as a function of spatial frequency. The imposition of mask functions with sharp cutoffs on both the original and reconstructed images was avoided, since this process results in high frequency components that correlate strongly to each other, giving too high values of the *FSC* function at these frequencies. In evaluating the *FSC* functions using equation (17), any anisotropy in the reconstructions due to a non-uniform distribution of projection directions was averaged out. This was not a limitation here since the comparison between exact and analytical filters was under identical geometrical conditions.

Another function relevant to the evaluation of reconstruction quality is the averaged radial power spectrum (*RPS*):

$$RPS(S) = 1/N(S) \sum_{R=S} |F(R)| \qquad (18)$$

where the sums are over all voxels at radius S in the 3*D* Fourier transforms, and the division (averaging) is by the number of voxels $N(S)$ in this shell. This function indicates how the information in a 3*D* image is distributed over the different spatial frequencies.

All programs were implemented in Fortran 77 within the framework of the IMAGIC image processing system [39], and run on a VAX 11/780 computer (Digital Equipment Corporation) under the VAX/VMS operating system.

Evaluation of exact filters – Results

The middle cross-sections of the 12 reconstructions are shown in fig. 7, for comparison with the corresponding middle cross-sections of the original images in fig. 7m and 7n. Visually, all reconstructions contain features corresponding to those in the original image. For both phantoms, simple back projection results in a very blurred reconstruction, due to the greater enhancement of low frequency information by this technique (fig. 7a, 7d, 7g, 7j). The necessity of boosting the relative contribution of the high frequency components becomes clear when examining these images. Filtered back projection using the analytical filter gives an image with apparently much finer features (fig. 7b, 7e, 7h, 7k). The reconstructions obtained by filtered back projection with exact filters appear slightly blurrier than those obtained using the analytical filter (fig. 7c, 7f, 7i, 7l).

Cross-correlation coefficients (*CCC*) between the 12 reconstructions and the original images are listed in table 1. Reconstructions obtained using simple back projection without filtering are the worst as indicated by this measure. For phantom A, the *CCC* is slightly better for the reconstruction obtained using the analytical filter than the exact filters. For phantom B, the reconstruction obtained using exact filter functions is the best as indicated by the *CCC*. As expected, the *CCC* confirms that better reconstructions are obtained using 200 rather than 59 projections.

The *CCC* and visual inspection by themselves are insufficient for us to make an appropriate evaluation of the use of exact filters. The Fourier shell correlation (*FSC*) functions for the eight reconstructions using filtered back projection are plotted in fig. 8. These functions indicate that exact filter functions give a reconstruction more closely resembling the original image for both phantoms and at nearly all spatial frequencies. Again as would be expected, a better reconstruction is obtained using 200 uniformly distributed projections than 59 nonuniformly distributed projections. The *FSC* functions for reconstructions with exact and analytical filters come together at the highest spatial frequencies. The *FSC* functions for reconstructions by simple back projection (not shown) generally coincided at low frequencies with the *FSC* functions of reconstructions with the analytical filter, and at higher frequencies the former curves lay below the latter ones.

Finally, the radial power spectra (*RPS's*) of both original phantoms and their reconstructions are presented in fig. 9. Fig. 9a shows the *RPS* of phantom A; all spatial frequencies are uniformly represented (white spectrum). Compared with the sorts of images that one encounters in practice [e.g., 38], this object contains an extraordinarily large proportion of high spatial frequency information.

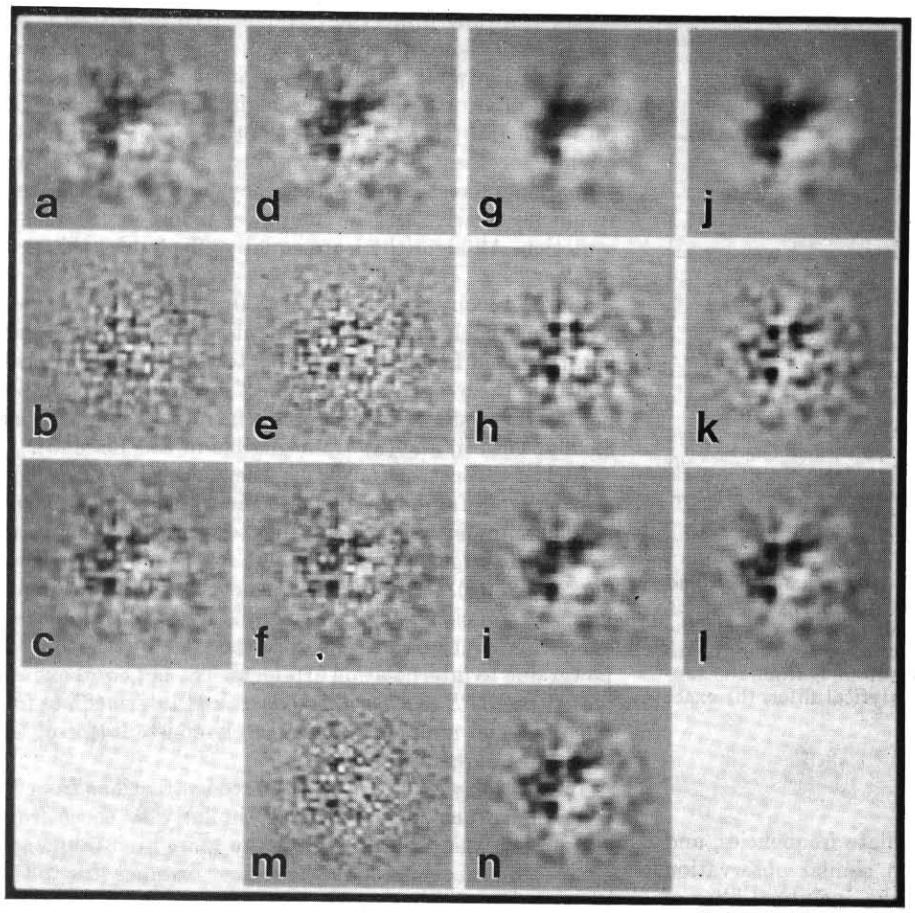

Fig. 7. Cross-sections of $3D$ reconstructions from:

(a) phantom A; 59 projections, no filter;
(b) phantom A; 59 projections, analytical filter;
(c) phantom A; 59 projections, exact filters;
(d) phantom A; 200 projections, no filter;
(e) phantom A; 200 projections, analytical filter;
(f) phantom A; 200 projections, exact filters;
(g) phantom B; 59 projections, no filter;
(h) phantom B; 59 projections, analytical filter;
(i) phantom B; 59 projections, exact filters;
(j) phantom B; 200 projections, no filter;
(k) phantom B; 200 projections, analytical filter;
(l) phantom B; 200 projections, exact filters.

The corresponding cross-sections of the original images:

(m) phantom A.
(n) phantom B.

For display in this figure only, the various images have been scaled to the same background density and variance.

Table 1. Cross-correlation coefficients between $3D$ reconstructions and the original $3D$ image.

Phantom	Number of Projections	No Filter	Analytical Filter	Exact Filters
A	59	0.442	0.688	0.678
A	200	0.501	0.834	0.778
B	59	0.702	0.831	0.938
B	200	0.750	0.944	0.972

Fig. 9e shows the *RPS* of phantom B which, due to the $3D$ Gaussian lowpass filter operation, contains much less high frequency power. In the rest of fig. 9, only the *RPS's* of reconstructions from 200 projections are shown.

In the reconstruction of phantom A obtained by simple back projection, the lowest spatial frequencies predominate and the *RPS* rapidly drops to zero (fig. 9b). As could be expected, the *RPS* of the reconstruction of phantom B drops even faster than that of the high frequency phantom A reconstruction (fig. 9f).

In the reconstruction of phantom A obtained by filtered back projection with the analytical filter, the *RPS* rises

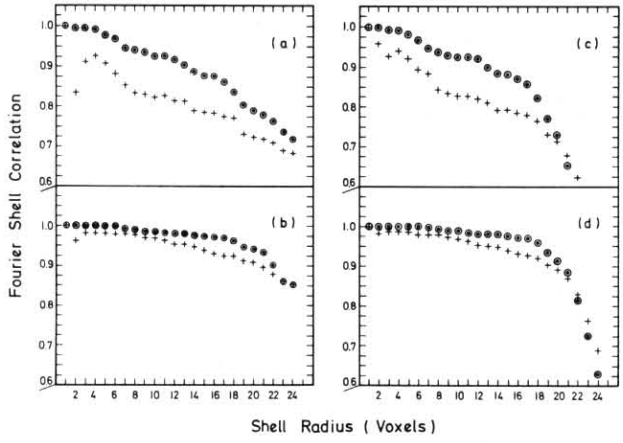

Fig. 8. Fourier shell correlation functions of reconstructions from:

(a) phantom A, 59 projections, analytical and exact filters;
(b) phantom A, 200 projections, analytical and exact filters;
(c) phantom B, 59 projections, analytical and exact filters;
(d) phantom B, 200 projections, analytical and exact filters.

The crosses mark values for analytical filter reconstructions. The circled dots mark values for reconstructions with exact filters. The circled crosses mark points where the two functions coincide.

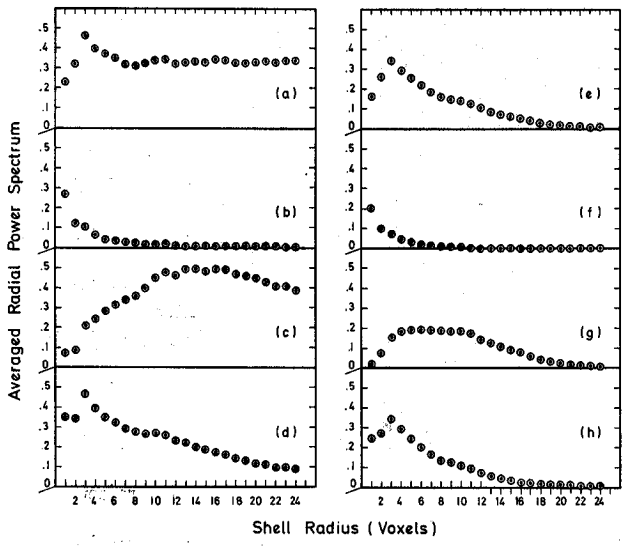

Fig. 9. Averaged radial power spectra of (a) phantom A, and 3*D* reconstructions of phantom A from 200 projections using (b) no filter, (c) the analytical filter, (d) exact filters. On the right hand side are averaged radial power spectra of (e) phantom B, and 3*D* reconstructions of phantom B from 200 projections using (f) no filter, (g) the analytical filter, (h) exact filters.

from zero to a flat peak at intermediate frequencies, and then slowly falls again (fig. 9c). A similar observation applies to the reconstruction with the analytical filter of phantom B, except for the smaller amount of high spatial frequency information (fig. 9g).

The *RPS's* of the reconstructions with exact filters of both phantoms A and B have a peak at low frequencies and then slowly fall (fig. 9d and 9h). The *RPS's* of these reconstructions are the ones most similar in shape and magnitude to the *RPS's* of the original images, except for the gradual falloff with increasing frequency.

Discussion – Radial power spectra

In this paper, we have discussed the design of filter functions to compensate for the over-representation of low frequency components as a result of overlapping central sections. There are, however, two other major factors which affect the radial power spectrum of a reconstruction:

(i) With a limited number of projections, there are gaps in the Fourier transform of the reconstruction between the central sections at higher spatial frequencies (fig. 1b). The total power at these frequencies is thus lower than in the original object because of the missing information. This effect is negligible in the case of 200 quasi-uniformly distributed projections [22], but is serious with only 59 projections (fig. 6).

(ii) In calculating the digital projections from the 3*D* object (forward projecting) and in reconstructing a 3*D* image from these projections (back projecting), a bilinear interpolation was used [34]. This interpolation acts as a lowpass filter, attenuating the high frequency spatial information [40] first of the 2*D* projections, and subsequently of the 3*D* reconstructions. The amount of attenuation increases with frequency, and at the highest frequency nearly 50% of the power is lost in the reconstruction. All algorithms are equally affected by this process.

In the reconstructions from 200 projections obtained by simple back projection without filtering (fig. 9b and 9f), the rapid falloff of the *RPS's* to zero is due predominantly to the over-representation of low frequency components as a result of overlapping central sections. The effects of both (i) and (ii) are negligible in this instance.

In the reconstructions with the analytical filter, not only the zero frequency but also the whole low frequency range are underweighted, leading to reconstructions with a relatively large proportion of high frequency information (fig. 9c and 9g). In the high frequency range, the measured Fourier coefficients are overweighted by a factor f^2. However, this overweighting is compensated by the loss in power due to interpolation artefacts. The net consequence is that the *RPS* reaches a flat plateau at intermediate frequencies, and remains approximately constant (for phantom A) at higher frequencies.

Interestingly, the *RPS's* of the reconstructions from 59 projections (not shown) behave similarly to those from 200 projections, even though many more high frequency components are missing in the former instance due to the larger influence of gaps. One would expect the total power in the high frequency ranges to drop relative to the power in the original phantom, due to (i) above. The analytical filter, however, boosts these high frequency components way beyond their real value and, as a net effect, the power remains constant. In other words, the analytical filter "corrects" for the missing Fourier coefficients by overweighting the measured ones. The overweighting of the high frequency range by the analytical filter is partly compensated by the low pass filter effect of the interpolation procedure, giving the fortuitous result (phantom A, 200 projections) that the high frequencies are boosted in nearly the right amount. In summary, reconstructions with analytical filters look "sharp" (high frequency texture) due to two effects: (a) the under-representation of very low frequency information, and (b) the over-representation of the very high frequency components.

In the reconstructions from 200 projections obtained using exact filters (fig. 9d and 9h), the *RPS's* at all frequencies follow the *RPS's* of the original images closely except for the high frequencies where the influence of the lowpass filtering due to interpolation is felt. In the reconstructions with exact filters from only 59 projections (*RPS's* not shown), the power loss with increasing frequency is due also to the missing Fourier components beyond the isotropic resolution limit [22]. The measured Fourier components beyond this limit are weighted by unity. Unlike the analytical filter, the exact filters cause no artificial boosting of high resolution information.

Discussion – Fourier shell correlation functions

The examination of the radial power spectra (*RPS's*) provides a basis for discussion of the Fourier shell correlations (*FSC*) functions between each of the reconstructions and the original images.

The *FSC* for the simple back projection reconstruction (not shown) is almost identical to the *FSC* for the analytical filter (fig. 8); only at very high frequencies are its values somewhat lower than for the analytical filter. The only difference between a simple back projection and the filtered back projection with the analytical filter, is that in the latter case Fourier coefficients are weighted as a function of their radial distance to the origin. Since, however, the *FSC* is normalised by the square root of the power at each radial frequency, such filtering does not affect the *FSC* and both *FSC's* are indeed virtually identical. Since the high frequency components are very weak in the reconstructions by simple back projection (fig. 9b and 9f), interpolation artefacts affect the image quality at these spatial frequencies more than with the analytical filter, explaining the slightly lower *FSC* curve in that region.

Reconstructions calculated with the analytical filter are underweighted in the low frequency range and overweighted in the very high frequency range. Since the weighting is radially symmetric, however, it does not affect the *FSC* function values. The *FSC* curves for the analytical filter lie below those for exact filters at all spatial frequencies (fig. 8) because the nonuniform distribution of projection directions is not taken into account with analytical filters. Only at the very high frequencies, where interpolation effects become predominant, do the *FSC* curves of the analytical and exact filter reconstructions merge.

The exact filter reconstructions lead to *FSC* functions that are indeed "exact" as was expected. The loss of high frequency power due to the interpolation effects may also be compensated for with exact filters. Interestingly, the overall quality of the reconstruction is a continuous function of the number of projections, much more so than would be expected from the resolution criteria for direct $3D$ reconstructions [22]. There is no sharp cutoff of information around the predicted value ("g"). Much rather, the quality of the reconstructions already starts degrading slowly at values lower than g, a process which continues up to values much higher than g. The *FSC* function is, of course, a more subtle quality indicator than g since it is not restricted to a single number.

The *FSC* functions, which are normalised at each spatial frequency, indicate that reconstructions obtained using exact filters are better at nearly all spatial frequencies than reconstructions obtained using the analytical filter. The *CCC*, however, provides a contradictory measure (table 1). The explanation for this is that simple picture similarity measures such as the cross-correlation coefficient are normally greatly affected by factors such as the relative proportions of high or low frequency data. Both phantom A and its reconstruction from projections with the analytical filter have strong high frequency components, leading to a good correlation value (table 1). Moreover, for a normal object containing a relatively small amount of high frequency information (phantom B), the *CCC* values are not all that different for the three algorithms tested here since they all reasonably reproduced the low frequency information. Simple picture similarity measures are also very sensitive to factors that do not really influence the information content of a reconstruction, e.g., multiplication by or addition of a constant value. This class of similarity measures is too lacking in information to be used for the comparison of 3D reconstruction algorithms.

The use of Fourier shell correlation functions and radial power spectra has enabled us to analyse in detail the frequency content of $3D$ reconstructions obtained using various filter functions. With *FSC* functions, we have demonstrated that the use of filters that are exact for each projection in a filtered back projection algorithm gives $3D$ reconstructions that correlate well with the original image, at all spatial frequencies. Moreover, the weighting of all frequency components is consistent with the representation of data at these frequencies by the projections available. At present, the methods outlined in this paper represent the most rational approach to $3D$ reconstruction from randomly oriented projections using the filtered back projection algorithm.

Conclusions

We have described the means of evaluating from basic principles filter functions for filtered back projection reconstruction algorithms. These filter functions are designed specifically to compensate for the overlap of information at all spatial frequencies by a given set of projection images, and can be computed using the same general approach for any particular reconstruction geometry, either tomographic or direct $3D$, and for any given number and angular distribution of projections. Each projection has a corresponding filter function that is based on its orientational relationship to all other projections. We have evaluated the use of exact filter functions using a new type of test object with a predefined power spectrum behaviour. We have also demonstrated that simple picture similarity measures such as the cross-correlation coefficient are poor measures of reconstruction quality, and that a more detailed analysis of the spatial frequency composition of the reconstruction is imperative. Using Fourier shell correlation functions, we have shown that reconstructions obtained using the exact filter functions are more faithful to the original image than reconstructions obtained with the more commonly used filter functions derived solely by analytical means. The filtered back projection algorithm with exact filters can thus be recommended for general geometry reconstruction problems from a finite number of projections.

Acknowledgements

We would like to thank Dr. Elmar Zeitler for his continuous support of our work. George Harauz is the recipient of a Postdoctoral Fellowship from the Medical Research Council of Canada.

References

[1] M. Zwick and E. Zeitler, Optik **38** (1973) 550.
[2] R. Gordon and G.T. Herman, Int. Rev. Cytol. **38** (1974) 111.
[3] R.A. Brooks and G. di Chiro, Phys. Med. Biol. **21** (1976) 689.
[4] G.T. Herman, Image Reconstruction from Projections, Academic Press, New York (1980).
[5] N.J. Pelc and D.A. Chesler, J. Comp. Assist. Tomog. **3** (1979) 385.
[6] J.G. Colsher, Phys. Med. Biol. **25** (1980) 103.
[7] J.B. Ra, C.B. Lim, Z.H. Cho, S.K. Hilal and J. Correll, Phys. Med. Biol. **27** (1982) 37.
[8] B. Schorr, D. Townsend and R. Clack, Phys. Med. Biol. **28** (1983) 1009.
[9] G. Harauz and F.P. Ottensmeyer, Ultramicroscopy **12** (1984) 309.
[10] G. Harauz, Nucleosome reconstruction via phosphorus mapping, Ph.D. Thesis, Department of Medical Biophysics, University of Toronto (May, 1984).
[11] M.G. van Heel and J. Frank, Ultramicroscopy **6** (1981) 187.
[12] M.G. van Heel, Ultramicroscopy **13** (1984) 165.
[13] G. Harauz and M. van Heel, in: E.S. Gelsema and L.N. Kanal (eds.), Pattern Recognition in Practice II, North-Holland, Amsterdam (1986) p. 279.
[14] G.N. Ramachandran and A.V. Lakshminarayanan, Proc. Nat. Acad. Sci. U.S.A. **68** (1971) 2236.
[15] B. Schorr and D. Townsend, Phys. Med. Biol. **26** (1981) 305.
[16] E. Tanaka, Phys. Med. Biol. **24** (1979) 157.
[17] M.G. van Heel, in: G.W. Bailey (ed.), Proceedings of the 41st Annual Meeting of the Electron Microscopy Society of America, San Francisco Press, San Francisco (1983) p. 460.
[18] G. Harauz and F.P. Ottensmeyer, Science **226** (1984) 936.
[19] A. Verschoor, J. Frank, M. Radermacher, T. Wagenknecht and M. Boublik, J. Mol. Biol. **178** (1984) 677.
[20] R.A. Crowther, D.J. DeRosier and A. Klug, Proc. Royal Soc. London A **317** (1970) 319.
[21] P.R. Smith, T.M. Peters and R.H.T. Bates, J. Phys. A **6** (1973) 361.
[22] M.G. van Heel and G. Harauz, "Resolution criteria for three dimensional reconstruction", Optik, this issue.
[23] W. Hoppe and R. Hegerl, in: P.W. Hawkes (ed.), Computer Processing of Electron Microscope Images, Springer-Verlag, Berlin (1980) p. 127.
[24] P.R. Smith, Ultramicroscopy **7** (1981) 155.
[25] L.A. Shepp and B.F. Logan, I.E.E.E. Trans. Nucl. Sci. **NS-26** (1974) 21.
[26] D.A. Chesler and S.J. Riederer, Phys. Med. Biol. **20** (1975) 632.
[27] Y.S. Kwoh, I.S. Reed and T.K. Troung, I.E.E.E. Trans. Nucl. Sci. **NS-24** (1977) 1990.
[28] E.T. Tsui and T.F. Budinger, I.E.E.E. Trans. Nucl. Sci. **NS-26** (1979) 2687.
[29] S. Suzuki, Optik **66** (1983) 61.
[30] S. Suzuki. Optik **67** (1984) 105.
[31] M. Radermacher and W. Hoppe, in: Proceedings of the 9th International Congress on Electron Microscopy, Toronto (1978) vol. 1, p. 218.
[32] D.C. Champeney, Fourier Transforms and Their Physical Applications, Academic Press, London and New York (1973).
[33] M.G. van Heel, in: Proceedings of the 8th European Congress on Electron Microscopy, Budapest (1984) vol. 2, p. 1347.
[34] G. Harauz and F.P. Ottensmeyer, Phys. Med. Biol. **28** (1983) 1419.
[35] H.C. Andrews, Introduction to Mathematical Techniques in Pattern Recognition, Wiley-Interscience, New York (1972) p. 143.
[36] W.O. Saxton and W. Baumeister, J. Microscopy **127** (1982) 127.
[37] M.G. van Heel, W. Keegstra, W. Schutter and E.F.J. van Bruggen, in: E.J. Wood (ed.), Structure and Function of Invertebrate Respiratory Proteins, Harwood Academic Publishers, Chur, (1982) p. 69.
[38] M.G. van Heel and M. Stöffler-Meilicke, EMBO Journal **4** (1985) 2389.
[39] M.G. van Heel and W. Keegstra, Ultramicroscopy **7** (1981) 113.
[40] W.K. Pratt, Digital Image Processing, Wiley, New York (1978).